The Astrophysical Journal, 945:57 (14pp), 2023 March 1 https://doi.org/10.3847/1538-4357/acb6fc

Global 3D Radiation Magnetohydrodynamic Simulations of Accretion onto a Stellar-mass Black Hole at Sub- and Near-critical Accretion Rates

Jiahui Huang[1], Yan-Fei Jiang (姜燕飞)[2], Hua Feng[3,1], Shane W. Davis[4], James M. Stone[5], and Matthew J. Middleton[6]
[1] Department of Engineering Physics, Tsinghua University, Beijing 100084, People's Republic of China
[2] Center for Computational Astrophysics, Flatiron Institute, New York, NY 10010, USA; yjiang@flatironinstitute.org
[3] Department of Astronomy, Tsinghua University, Beijing 100084, People's Republic of China; hfeng@tsinghua.edu.cn
[4] Department of Astronomy, University of Virginia, Charlottesville, VA 22904, USA
[5] School of Natural Sciences, Institute for Advanced Study, Princeton, NJ 08544, USA
[6] Department of Physics & Astronomy, University of Southampton, Southampton, SO17 1BJ, UK
Received 2022 September 8; revised 2023 January 24; accepted 2023 January 26; published 2023 March 7

Abstract

We present global 3D radiation magnetohydrodynamic simulations of accretion onto a 6.62 solar-mass black hole, with quasi-steady-state accretion rates reaching 0.016–0.9 times the critical accretion rate, which is defined as the accretion rate for powering the Eddington luminosity, assuming a 10% radiative efficiency, in three different runs. The simulations show no sign of thermal instability over hundreds of thermal timescales at $10\,r_{\rm g}$. The energy dissipation occurs close to the mid-plane in the near-critical runs and near the disk surface in the low–accretion rate run. The total radiative luminosity inside $\sim 20\,r_{\rm g}$ is about 1%–30% of the Eddington limit, with radiative efficiencies of about 6% and 3%, respectively, in the sub- and near-critical accretion regimes. In both cases, self-consistent turbulence generated by the magnetorotational instability leads to angular momentum transfer, and the disk is supported by magnetic pressure. Outflows from the central low-density funnel, with a terminal velocity of $\sim 0.1c$, are seen only in the near-critical runs. We conclude that these magnetic pressure–dominated disks are thermally stable and thicker than the α disk, and that the effective temperature profiles are much flatter than those in the α disks. The magnetic pressures of these disks are comparable within an order of magnitude to the previous analytical magnetic pressure–dominated disk model.

Unified Astronomy Thesaurus concepts: Accretion (14); Radiative magnetohydrodynamics (2009); Magnetohydrodynamical simulations (1966); Stellar mass black holes (1611)

1. Introduction

X-ray binaries are among the most luminous X-ray objects in the Milky Way and in nonactive galaxies (Remillard & McClintock 2006). Their total luminosity is scaled with the star formation rate and the total stellar mass of the host galaxy (Gilfanov 2004; Mineo et al. 2012). They are responsible for the heating of the intergalactic medium during the epoch of reionization in the early universe (Jeon et al. 2014). Powered by accretion onto black holes or neutron stars, X-ray binaries exhibit strong radiation and a variety forms of outflows (Done et al. 2007). Thus, studying the accretion helps us to understand how the radiation and outflows are generated, their interactions with the environment, and the fundamental properties of the central compact object.

However, the physics accompanying accretion has not yet been fully understood. If the accretion rate is low, then the accretion flow is believed to be hot and optically thin (Yuan & Narayan 2014). With a moderate accretion rate, the X-ray spectra of X-ray binaries can reasonably be described with the standard accretion disk model (Shakura & Sunyaev 1973), in which the viscous heat is balanced by local radiation, predicting an optically thick yet geometrically thin multicolor disk. In the high-accretion regime, i.e., when the accretion is close to or exceeds the rate needed to power the Eddington luminosity, both advection and outflows are expected to take place, and the disk could be highly turbulent. In such a case, no valid analytic models exist to account for all these issues. The slim disk model (Abramowicz et al. 1988), which assumes advection rather than radiation to be the dominant cooling mechanism, is found to be stable at high accretion rates, and has been used to fit the energy spectra of luminous X-ray binaries (Watarai et al. 2001). However, the model remains incomplete with a consideration of the radiation-driven outflows (Poutanen et al. 2007) that have been ubiquitously observed in (ultra)luminous X-ray binaries (Neilsen & Lee 2009; Middleton et al. 2014, 2015; Pinto et al. 2016; Kosec et al. 2021).

The magnetic field should play an essential role in transporting the angular momentum (Balbus & Hawley 1991) and possibly also supporting the disk (Pariev et al. 2003), in addition to the thermal and radiation pressure, although usually only the latter two phenomena are considered in analytical models. The standard disk model is found to be thermally unstable if radiation pressure dominates (Shakura & Sunyaev 1976), while the slim disk is stable when advection becomes the major cooling term. Begelman & Pringle (2007) have suggested that the disk could be supported by the magnetic pressure, which saturates when the magnetorotational instability (MRI) is sufficiently developed.

During the outbursts of X-ray binaries, one also needs to assume a hot corona, to account for the observed hard Comptonized X-rays in addition to the soft thermal photons originating in the optically thick multicolor disk. The formation of the corona has been discussed analytically, as, e.g., a magnetically driven corona (Galeev et al. 1979) or a radiation-

evaporated corona (Meyer & Meyer-Hofmeister 1994; Esin et al. 1997). Some observations have suggested that the corona is related to the jet base (Markoff et al. 2005). Massive numerical simulations have shown the presence of hot gaseous coronas (Morales Teixeira et al. 2018; Jiang et al. 2019a; Kinch et al. 2020). Recently, X-ray polarization observations with PolarLight (Long et al. 2022) and the Imaging X-ray Polarimetry Explorer (Krawczynski et al. 2022) have placed constraints on corona geometry. Also, in order to incorporate the jet formation, one has to rely on numerical simulations (Davis & Tchekhovskoy 2020).

It is challenging to resolve the thin disk with numerical simulations in the subcritical regime. Hawley (2001) and Hawley & Krolik (2001) have performed global magneto-hydrodynamic (MHD) simulations of the thin disk, without considering any radiation effects. Hogg & Reynolds (2016, 2018) have added an artificial cooling function, to approximate the radiation transfer and keep the accretion disk thin. In the meantime, general relativity magnetohydrodynamic (GR-MHD) simulations (De Villiers et al. 2003; Koide 2003; McKinney & Gammie 2004; Shafee et al. 2008; Noble et al. 2009; Schnittman et al. 2013) have been carried out to investigate the accretion flow in the Kerr metric. The above simulations have mainly focused on the estimation of the accretion efficiency and the stress-to-pressure ratio of the thin disks. Ohsuga (2006) conducted a 2D radiation hydrodynamic (RHD) simulation of an assumed α disk, with radiation transfer being taken into account. Their simulation had a large mass input rate of 100 $L_{\rm Edd}/c^2$, such that the disk did not always stay in the sub-Eddington thin disk state, but displayed super-Eddington bursts. Recently, Morales Teixeira et al. (2018) have presented a global simulation of a subcritical thin disk with 3D GR-RMHD codes in the magnetically arrested disk state, with treatment of radiation transport. Fragile et al. (2018) have presented a 2D GR-RHD simulation of a viscous Shakura–Sunyaev thin accretion disk around a stellar-mass black hole, employing the M1 scheme for the radiation.

In recent years, more attention has been paid to the simulation of systems with high accretion rates. These simulations can be classified into three categories. The 2D simulations can be expanded to large radii, for the large-scale structures of the accretion flow to be studied, thanks to the fewer computational resources that are needed. However, because of the antidynamo theorem, the 2D simulations cannot sustain MRI turbulence self-consistently. As a result, they are either purely RHD, with a viscosity assumption (Kawashima et al. 2009; Hashizume et al. 2015; Kitaki et al. 2017, 2018, 2021; Ogawa et al. 2017), or they are RMHD, with a mean-field dynamo approximation (Ohsuga et al. 2009; Ohsuga & Mineshige 2011; Sądowski et al. 2015). The 3D GR-RMHD simulations are resource-consuming: they can only resolve the innermost region of the accretion flow, but they offer an opportunity to study the impact of the black hole spin on accretion; they use the M1 scheme (Fragile et al. 2014; McKinney et al. 2014; Sądowski 2016; Takahashi et al. 2016; Wielgus et al. 2022) or a variable Eddington tensor (Asahina & Ohsuga 2022) to handle the radiation transport.

Our simulations adopt the pseudo-Newtonian potential, but solve the full angular-resolved transport equation without assuming the closure relation. Using the same codes, Jiang et al. (2014a) have performed simulations of a supercritical accretion flow around a stellar-mass black hole in cylindrical coordinates. Similar simulations in spherical coordinates have been conducted for subcritical (Jiang et al. 2019a) and supercritical (Jiang et al. 2019b) accretion onto a supermassive black hole. In this paper, we present the results from 3D RMHD simulations of the accretion flows around a stellar-mass black hole, in spherical coordinates, with different initial conditions, leading to various accretion rates, from sub- to near-critical accretion rates. We try to extract the accretion properties—such as the radiative efficiency, outflow rate, disk structure, and corona temperature—as a function of the accretion rate, and we analyze the mechanism for angular momentum transfer under different accretion rates.

The paper is organized as follows. We describe the simulation setup in Section 2. The main features of the accretion flows from the simulations are presented in Section 3, including the time variations (3.2), the inflow and outflow rates (3.3), the radiation and advection luminosities (3.4), the 2D disk structure (3.5), and the 1D radial (3.6) and vertical (3.7) disk structures. The results are discussed in Section 4, and summarized in Section 5.

2. Simulation Setup

We adopt ideal MHD with radiative transfer in the simulation, using the same equations as in Jiang et al. (2019b; see their Equations (1)–(6)). We carry out the simulations using the code Athena++ (Stone et al. 2019) and the method described in Jiang (2021). We assume the pseudo-Newtonian potential (Paczyński & Wiita 1980), to mimic the effect of general relativity around a Schwarzschild black hole:

$$\phi = -\frac{GM_{\rm BH}}{r - 2r_{\rm g}}, \tag{1}$$

where G is the gravitational constant and $r_{\rm g} \equiv GM_{\rm BH}/c^2$ is the gravitational radius. The Compton scattering effect is treated based on the difference between the radiation and gas temperatures. The interactions between the gas and the radiation are described by a source term in the radiation transport equation, as in Jiang et al. (2019b; see their Equation (4)).

We carry out three runs of simulations—namely XRB0.01, XRB0.8, and XRB0.9—around a 6.62 $M_\odot$ stellar-mass black hole. The fiducial parameters used in the simulation are listed in Table 1. We initialize a hydrostatic rotating gas torus, with a density maximum at 120 $r_{\rm g}$ and different maximum gas densities and temperatures. The shape of the gas torus is the same as that in Jiang et al. (2019b) and Jiang et al. (2019a). The inner edge of the torus is at 60 $r_{\rm g}$, and we fill the region outside the initial torus with a density floor of 10^{-8} ρ_0. The initial parameters—including the maximum density $\rho_{\rm i}$, the maximum gas temperature $T_{\rm i}$, and the ratio between the radiation pressure $P_{\rm R}$ and the magnetic pressure $P_{\rm B}$ to the gas pressure $P_{\rm g}$—are summarized in Table 2. The three runs assume different initial magnetic field configurations. Magnetic fields with a single loop are adopted in run XRB0.9, while those with multiple loops are used in runs XRB0.01 and XRB0.8; see Figure 1 for an illustration. The different initial parameters and the different magnetic field configurations lead to different mass accretion rates for the disks formed near the central black hole.

The simulation covers the domain of $(r, \theta, \phi) \in (4r_{\rm g}, 1600r_{\rm g}) \times (0, \pi) \times (0, 2\pi)$. The highest resolution

Table 1
Fiducial Simulation Parameters

Parameter	Definition	Value	Physical Meaning
$M_{\rm BH}$	$6.62M_{\odot}$	1.32×10^{34} g	Black hole mass
$r_{\rm g}$	$GM_{\rm BH}/c^2$	9.76×10^{5} cm	Gravitational radius
$\kappa_{\rm es}$		0.34 g^{-1} cm^2	Electron-scattering opacity
$L_{\rm Edd}$	$4\pi GM_{\rm BH}c/\kappa_{\rm es}$	9.74×10^{38} erg s^{-1}	Eddington luminosity
$\dot{M}_{\rm crit}$	$10L_{\rm Edd}/c^2$	1.08×10^{19} g s^{-1}	Critical accretion rate
ρ_0		10^{-2} g cm^{-3}	Fiducial density
T_0		10^{7} K	Fiducial temperature
P_0	$R_{\rm ideal}\rho_0T_0$	1.39×10^{13} dyn cm^{-2}	Fiducial pressure
v_0	$\sqrt{R_{\rm ideal}T_0}$	3.73×10^{7} cms^{-1}	Fiducial velocity
t_0	$2r_g/v_0$	5.23×10^{-2} s	Fiducial time
B_0	$\sqrt{P_0}$	3.73×10^{6} G	Fiducial magnetic field
E_0	$a_{\rm R}T_0^4$	7.57×10^{13} erg cm^{-3}	Fiducial radiation energy density
F_0	cE_0	2.27×10^{24} erg cm^{-2} s^{-1}	Fiducial radiation flux

Note. We assume an accretion efficiency of 0.1, to relate the critical accretion rate to the Eddington limit. $R_{\rm ideal}$ is the ideal gas constant, with a mean molecular weight $\mu = 0.6$. $a_{\rm R} = 7.57\times10^{-15}$ erg cm^{-3} K^{-4} is the radiation constant.

Table 2
Initial Simulation Parameters

Variable/Units	XRB0.01	XRB0.8	XRB0.9
$r_{\rm i}/r_{\rm g}$	120	120	120
$\rho_{\rm i}/\rho_0$	0.05	6	10
$T_{\rm i}/T_0$	1.38	4.55	5.16
$\langle P_{\rm R}/P_{\rm g}\rangle$	5.22×10^{3}	53.6	35.6
$\langle P_{\rm R}/P_{\rm g}\rangle_\rho$	2.50×10^{2}	22.1	19.2
$\langle P_{\rm B}/P_{\rm g}\rangle$	2.95×10^{-2}	2.10×10^{-4}	1.34×10^{-3}
$\langle P_{\rm B}/P_{\rm g}\rangle_\rho$	1.18×10^{-2}	6.22×10^{-5}	3.97×10^{-4}
$\Delta r/r$	0.012	0.012	0.012
$\Delta\theta$	0.012	0.012	0.012
$\Delta\phi$	0.012	0.012	0.012
$N_{\rm n}$	80	80	80

Note. The center of the initial torus is at $r_{\rm i}$. The initial density and the gas temperature at the center of the torus are $\rho_{\rm i}$ and $T_{\rm i}$, respectively. For any quantity a, $\langle a\rangle$ is the volume-averaged value inside the initial gas torus and $\langle a\rangle_\rho$ is the density-weighted average value inside the torus. The grid sizes Δr, $\Delta\theta$, and $\Delta\phi$ are for the finest grids at the center of the torus. The numbers of angles for the radiation grid are $N_{\rm n}$ in each cell.

reaches $\Delta r/r = \Delta\theta = \Delta\phi = 0.012$ near the disk mid-plane. We use 80 discrete angles in each cell to resolve the angular distribution of the radiation field.

3. Results

The MRI creates turbulence in the initial mass torus and transports angular momentum outward. The mass is slowly accreted onto smaller radii and forms an accretion disk self-consistently. Due to the different initial magnetic fields, and thus the different magnitudes of the MRI and angular momentum transfer rates, the three runs lead to distinct mass accretion rates. XRB0.01 has a subcritical ($\sim10^{-2}$ $\dot{M}_{\rm crit}$) accretion rate with sub-Eddington emission, while XRB0.8 and XRB0.9 are near-critical (0.8–0.9 $\dot{M}_{\rm crit}$)[7] and sub-Eddington. After the initial transition phase, the simulation converges to a quasi-steady state, during which the net accretion rate is relatively constant. If the standard deviation of the net accretion rate over a time span is less than one-third of the average, we define this period as the quasi-steady state and perform the analysis on it.

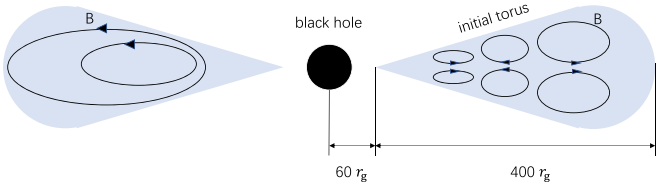

Figure 1. The initial torus and magnetic field configurations used in the simulations. The left side shows the initial setup, with single-loop magnetic fields (XRB0.9), while the right side shows the cases with multiple loops (XRB0.01 and XRB0.8).

3.1. Resolution for MRI Turbulence

To determine whether the MRI turbulence is adequately built and well resolved, we calculate the quality factors Q_θ and Q_ϕ, following Hawley et al. (2011) and Sorathia et al. (2012). The quality factor is defined as the ratio between the fastest-growing MRI mode $\lambda = 2\pi\sqrt{16/15}\,|v_{\rm A}|/\Omega$ and the cell sizes $r\triangle\theta$ or $r\sin\theta\triangle\phi$, respectively, along θ or ϕ, where $v_{\rm A}$ represents the Alfvén velocity for B_θ or B_ϕ. The statistical properties of the MRI turbulence do not change with the grid resolution if $Q_\theta \geqslant 6$, $Q_\phi \geqslant 25$, or both are greater than 10 (Hawley et al. 2013). We regard this as the condition for well-resolved MRI turbulence.

We calculate the azimuthally averaged quality factor in the three runs at radii from 6 to 20 $r_{\rm g}$. For XRB0.01, Q_θ is always larger than 15 near the disk surface, and it reduces from 8 at 6 $r_{\rm g}$ to 6 at 20 $r_{\rm g}$, near the disk mid-plane. For XRB0.8, Q_θ is found to be greater than 15 everywhere. For XRB0.9, Q_θ reduces from 10 at 6 $r_{\rm g}$ to 6 at 20 $r_{\rm g}$, near the disk mid-plane, but is occasionally found to be smaller than 6 in some small regions. Q_ϕ is over 50 in all the runs. Thus, $Q_\theta \geqslant 6$ and $Q_\phi \geqslant 25$ are satisfied in the majority of the central disk, e.g., the regions with grid refinement.

3.2. Simulation Histories

We calculate the net mass accretion rate at radius r as

$$\dot{M} = \int_0^{2\pi}\int_0^{\pi} \rho v_r r^2 \sin\theta d\theta d\phi. \quad (2)$$

The histories of $\dot{M}$ at 10 $r_{\rm g}$ for the three runs are shown in Figure 2. After an initial transition phase of 25–55 t_0 for each run, the accretion flows reach a quasi-steady state, which lasts for 20–40 t_0. We emphasize that the MRI turbulence in the quasi-steady state should be well resolved. For instance, although the mass accretion rate in XRB0.8 seems steadier over 20–50 t_0 than over 55–75 t_0, the MRI turbulence quality factors in the former interval are not high enough to justify a quasi-

[7] Strictly speaking, XRB0.8 and XRB0.9 are also subcritical, but we refer them as "near-critical" to distinguish them from XRB0.01.

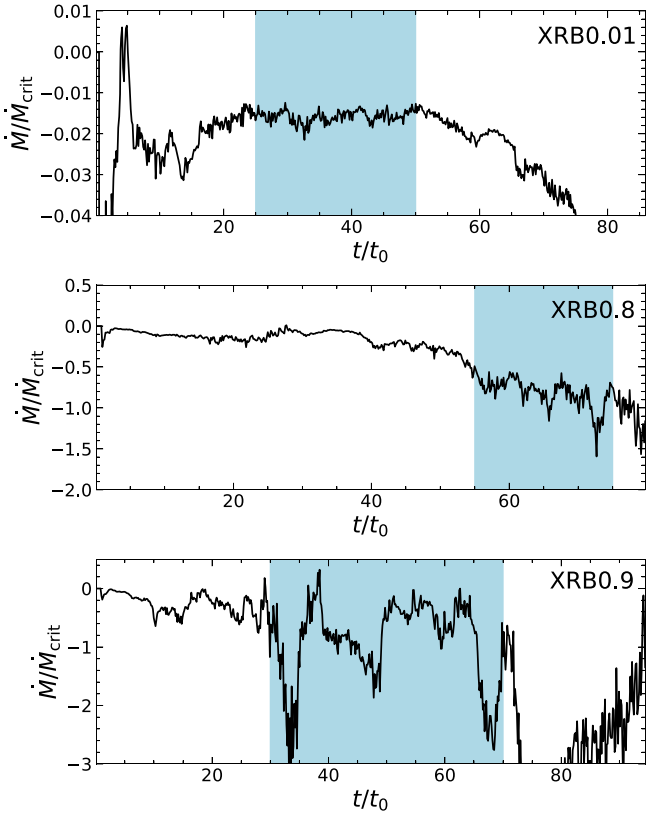

Figure 2. Histories of the spherically integrated mass accretion rates for the three runs at 10 $r_{\rm g}$. Negative means that gas flows toward the black hole. The quasi-steady states are marked by the blue shading. The accretion flows show no sign of thermal runaway over hundreds of thermal timescales at 10 $r_{\rm g}$.

steady state. The Keplerian rotation period of the Paczyński–Wiita potential at the radius r is (Jiang et al. 2014a)

$$t_{\rm K} = 1510\frac{r_{\rm g}}{c}\left(\frac{r}{40r_{\rm g}}\right)^{1/2}\left(\frac{r/2r_{\rm g}-1}{19}\right). \quad (3)$$

Therefore, the duration of each run is equivalent to ∼800 orbits at 10 $r_{\rm g}$. Over hundreds of thermal timescales at 10 $r_{\rm g}$, there is no sign of thermal instability for the three runs. The mass accretion rates in the quasi-steady state have significant fluctuations because of the MRI turbulence. The average accretion rates of the three runs are listed in Table 3. The standard deviations of the net accretion rates in XRB0.01, XRB0.8, and XRB0.9 are 9.4%, 21.2%, and 76.8%, respectively. In general, the standard deviation in the quasi-steady state is larger when the accretion rate is higher, while XRB0.9 has a significantly larger standard deviation, due to the rapid variations of the accretion rate at times around 33 t_0, 48 t_0, and 68 t_0, which are caused by the variations of the magnetic field strength (see the fuller discussion later in this section). If we omit these time intervals and only consider those with a relatively steady accretion rate, the standard deviation becomes 12.8% and 53.3%, respectively, over 40–45 t_0 and 51–63 t_0. The fluctuation of the accretion rate is linked with the topology of the initial magnetic field. For the runs XRB0.01 and XRB0.8, quadruple magnetic fields with a net $\bar{B}_r$ component are assumed. The net $\bar{B}_r$ near the mid-plane will shear into toroidal magnetic fields and quickly build up a strong magnetic pressure, which will escape from the mid-plane, due to magnetic buoyancy. The MRI turbulence shows less variability in these cases (Pessah & Psaltis 2005; Das et al. 2018) than in the case where the initial magnetic field has a single loop, i.e., in XRB0.9.

The histories of the azimuthally averaged profiles (spacetime diagrams) as a function of θ for the three runs are displayed in Figure 3, for the density ρ, the gas temperature T, and the azimuthal magnetic field component B_ϕ, at 20 $r_{\rm g}$. When the simulation enters the quasi-steady state at 20 $r_{\rm g}$ (marked between the two vertical black lines), there is a clear positive correlation between the disk scale height and the mass accretion rate. The locations of the photosphere for effective absorption (the green curves) and electron scattering (the blue curves), which are integrated from the rotational axis, are shown on top of the density profiles; their heights are also scaled with the accretion rate. High-temperature coronas (10^8–10^9 K) can be seen above the electron-scattering photospheres, consistent with the previous global simulations (Jiang et al. 2019a, 2014a) and local shearing-box simulations (Jiang et al. 2014b). For the XRB0.9 run, which initially has single-loop magnetic fields, B_ϕ repeatedly flips its direction near the disk mid-plane every 10 t_0 after the disk enters the quasi-steady state, which is roughly ∼30 Keplerian rotation periods at 20 $r_{\rm g}$. The magnetic buoyancy drives the matter with a strong magnetic field up from the disk mid-plane, forming the so-called butterfly diagram. The butterfly diagram has been observed in previous global simulations (Jiang et al. 2014a, 2019b, 2019a) and local shearing-box simulations (Stone et al. 1996; Miller & Stone 2000; Davis et al. 2010; Shi et al. 2010; Simon et al. 2012; Jiang et al. 2013, 2014b; Salvesen et al. 2016a, 2016b), and is believed to be related to a dynamo process of the MRI (Brandenburg et al. 1995; Blackman 2012). The butterfly diagram is not seen in the XRB0.01 or XRB0.8 runs, which initially have quadruple magnetic fields, because their magnetic fields have a net radial component near the disk mid-plane, and this component always transfers to B_ϕ in the same direction, by means of MRI.

In the XRB0.9 run, when the magnetic field flips its sign and reaches a minimum strength, the disk shrinks to a small scale height, suggesting that the disk is supported by magnetic pressure in this near-critical case. The details of the disk pressure will be discussed in Sections 3.6 and 3.7. Meanwhile, when the magnetic field strength reaches a maximum value, the angular momentum transport of the MRI turbulence is enhanced, and the accretion rate shows a sudden increase (see Figures 2 and 3).

3.3. Inflow and Outflow Rates

We calculate the time-averaged net mass accretion rate as a function of radius using the following equation:

$$\langle \dot{M} \rangle = \frac{1}{\Delta t}\int_0^{2\pi}\int_0^{\pi}\int_{t_1}^{t_2} \rho v_r r^2 dt \sin\theta d\theta d\phi, \quad (4)$$

where $\Delta t = t_2 - t_1$ is the time duration of the quasi-steady state. The radial profiles for the three runs are shown in Figure 4. The net mass accretion rate remains roughly constant up to 20 $r_{\rm g}$ for the XRB0.01 run and up to 26 $r_{\rm g}$ for the XRB0.8 and XRB0.9 runs; these are the radial ranges where the quasi-steady state is obtained. According to Equation (4), we are averaging over cells with both inward- and outward-moving gases. Therefore,

Table 3
Mass Rates, Powers, Temperatures, and Other Key Properties of the Accretion in the Three Runs

(1)	$\frac{\dot{M}}{\dot{M}_{\rm crit}}$ (2)	$\frac{L_{\rm R}}{L_{\rm Edd}}$ (3)	$\frac{L_{\rm k}}{L_{\rm Edd}}$ (4)	$\frac{L_{\rm R,BH}}{L_{\rm Edd}}$ (5)	$\frac{L_{\rm k,BH}}{L_{\rm Edd}}$ (6)	$\frac{\dot{M}_{\rm w}}{\dot{M}_{\rm crit}}$ (7)	$\eta_{\rm R}$ (8)	$\eta_{\rm R,BH}$ (9)	$\xi_{\rm w}$ (10)	$\theta_{\rm d}$ (11)	$T_{\rm c}$ (12)	$T_{\rm ph}$ (13)	$\frac{T_{\rm axis}}{\rm K}$ (14)	$\frac{v_{\rm w}}{c}$ (15)
XRB0.01	−0.0158	0.0096	0	−0.00068	−0.034	0	6.1%	0.4%	0	20°	$r^{-0.57}$	$r^{-0.59}$	3×10^9	
XRB0.8	−0.82	0.22	0.0023	−0.085	−1.6	0.021	2.6%	1.0%	2.5%	56°	$r^{-0.38}$	$r^{-0.44}$	2×10^9	0.122
XRB0.9	−0.9	0.34	0.0059	−0.091	−2.3	0.025	3.7%	1.0%	2.7%	73°	$r^{-0.48}$	$r^{-0.29}$	8×10^8	0.096

Note. Column (1): run name. Column (2): normalized net mass accretion rate. Column (3): normalized radiation luminosity. Column (4): normalized kinematic luminosity. Column (5): normalized radiation luminosity swallowed by the central black hole. Column (6): normalized kinematic luminosity swallowed by the central black hole. Column (7): normalized wind mass-loss rate. Column (8): the efficiency of the radiation. Column (9): the efficiency of the swallowed radiation. Column (10): the ratio of the true outflow mass rate to the net accretion rate. Column (11): the half-open angle of the effective absorption photosphere, or the central low-density funnel, measured from the disk mid-plane. Column (12): the mid-disk temperature as a function of radius. Column (13): the radial temperature profile of the effective absorption photosphere. Column (14): corona temperature. Column (15): maximum wind/outflow velocity.

the net mass accretion rate can be divided into the two components. We calculate the mass outflow rate by integrating cells with $v_r > 0$ and we calculate the mass inflow rate by integrating over those with $v_r < 0$. The mass outflow and inflow rates are also shown in Figure 4, by the blue and red curves. We note that the outflow, defined in this way, includes the true outflows that will escape to infinity, the failed outflows (Kitaki et al. 2021) that will eventually fall back onto the accretion disk at larger radii, and the turbulence inside the accretion disk. The turbulent fluctuations are the dominant component, more than an order of magnitude higher than the other two components. Both the mass outflow and inflow rates are much larger than the net mass accretion rate $\dot{M}$. The outgoing gas emerges outside the innermost stable circular orbit (ISCO), and the mass-loss rate quickly increases with radius. We find that the mass inflow and outflow rates are significantly smaller than in the active galactic nucleus (AGN) case, as expected by Jiang et al. (2019b). Note that our simulation does not take into account the effects of general relativity, thus the central black hole is nonrotating. Therefore, the outflows seen near the ISCO are driven by radiative and magnetic forces, but have no contribution from the Blandford–Znajek mechanism (Blandford & Znajek 1977).

3.4. Luminosity and Advection

To estimate the total radiative flux and the kinetic energy that is carried away by the true outflow, which is the outflow that can escape to infinity, we perform the integration through a cylindrical surface. The radius of the surface is set as the outer radius of the quasi-steady disk, such that the accretion flow within it has reached the quasi-steady state. The total radiative luminosity $L_{\rm R}$, the kinetic luminosity $L_{\rm k}$, and the true outflow mass flux $\dot{M}_{\rm w}$ are respectively calculated as

$$\begin{aligned} L_{\rm R} &= \int_0^{r_0} 2\pi F_{{\rm R},z} r dr + \int_{-z_0}^{z_0} 2\pi F_{{\rm R},r} r_0 dz, \\ L_{\rm k} &= \int_0^{r_0} 2\pi v_z \left(\frac{1}{2}\rho v^2\right) r dr + \int_{-z_0}^{z_0} 2\pi v_r \left(\frac{1}{2}\rho v^2\right) r_0 dz, \\ \dot{M}_{\rm w} &= \int_0^{r_0} 2\pi \rho v_z r dr + \int_{-z_0}^{z_0} 2\pi \rho v_r r_0 dz, \end{aligned} \tag{5}$$

where r_0 and z_0 are the radius and the half height of the cylindrical surface, and $F_{\rm R}$ is the radiation flux. We integrate through both the upper and lower sides of the disk. Only positive $F_{{\rm R},r}$ and v_r are considered in the integration, in order to exclude the inflow component of the turbulent disk. For $L_{\rm k}$ and $\dot{M}_{\rm w}$, we only include cells where the sum of the kinetic and gravitational energy is positive, implying that the gas will escape to infinity and be a true outflow. The time average is conducted during the quasi-steady state.

To find the suitable half height for the integration, we raise z_0 to see how it affects the radiative and kinetic luminosities. For the three runs, the radiative luminosity $L_{\rm R}$ saturates at 400–1000 $r_{\rm g}$, while the kinetic luminosity $L_{\rm k}$ saturates at 1500 $r_{\rm g}$. Thus, these z_0 are used for the integration. The radiation and outflows at these heights mainly come from the innermost quasi-steady area, according to the large-scale streamlines of velocity and radiation flux. The luminosities calculated in this section only represent the lower limits of their true values, because the integrated radiative and mechanical luminosities for these runs increase exponentially with radius beyond the quasi-steady region. In the wind, the radiative and internal energy may be converted to mechanical energy and drive more gases to escape to infinity. Thus, we also try to include cells where the total energy $E_{\rm t} = \frac{1}{2}\rho v^2 + \frac{\gamma P}{\gamma - 1} + \rho\phi + \frac{E_{\rm R}}{3}$ is higher than zero. $L_{\rm k}$ and $\dot{M}_{\rm w}$ will increase by a factor of about 2, if we consider the possible conversion of energy. On the contrary, an inverse conversion of energy may lower $L_{\rm k}$ and $\dot{M}_{\rm w}$. We define the lower limit of the radiative efficiencies as $\eta_{\rm R} = -L_{\rm R}/(\dot{M}c^2)$. The ratio of the true outflow rate to the net accretion rate that goes through the ISCO is calculated as $\xi_{\rm w} = -\dot{M}_{\rm w}/\dot{M}$. The luminosities and efficiencies of the three runs are listed in Table 3.

Advection of radiative and kinetic energy is an important cooling mechanism for accretion flows with high accretion rates. To evaluate the level of advection, we calculate the radiative energy $L_{\rm R,BH}$ and the kinetic energy $L_{\rm k,BH}$, which are swallowed by the central black hole. The integration is computed through a spherical surface at the ISCO as

$$\begin{aligned} L_{\rm R,BH} &= \int_0^{2\pi}\int_0^{\pi} F_{{\rm R},r}(6r_{\rm g})^2 \sin\theta d\theta d\phi, \ \text{and} \\ L_{\rm k,BH} &= \int_0^{2\pi}\int_0^{\pi} v_r\left(\frac{1}{2}\rho v^2\right)(6r_{\rm g})^2 \sin\theta d\theta d\phi, \end{aligned} \tag{6}$$

over cells with negative $F_{{\rm R},r}$ and v_r, to only include the inflow part. The swallowed radiative fraction of the accretion flow is defined as $\eta_{\rm R,BH} = L_{\rm R,BH}/(\dot{M}c^2)$. The swallowed power and its fractions in the three runs are listed in Table 3.

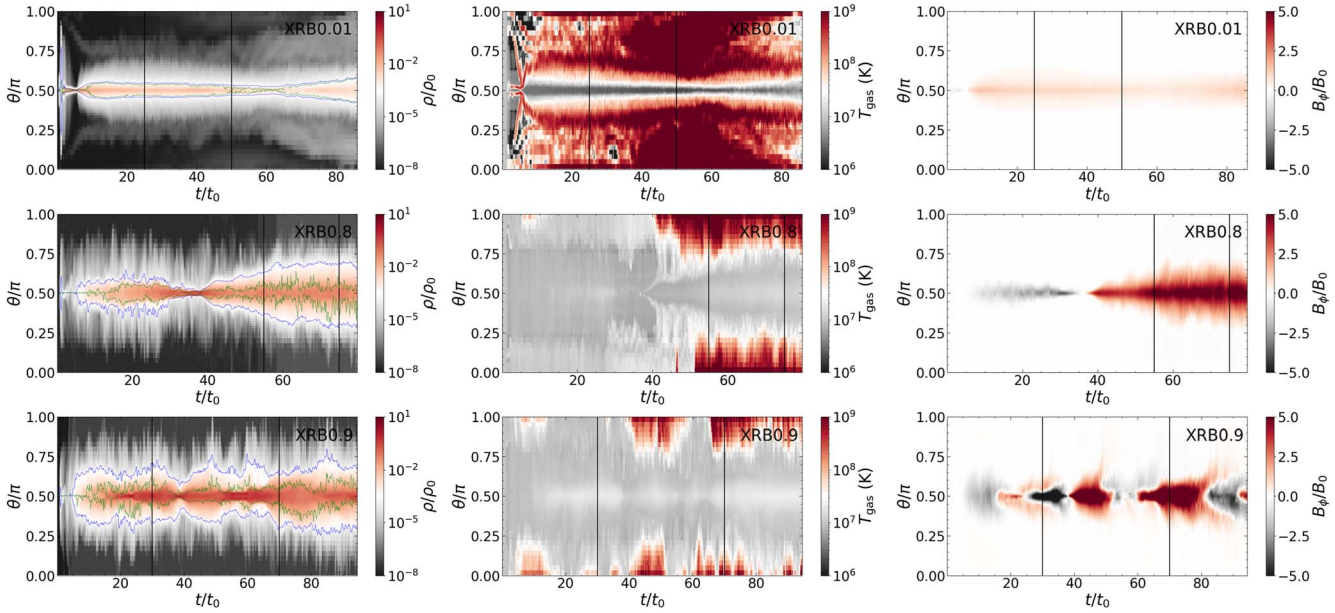

Figure 3. Spacetime diagrams of the azimuthally averaged density (left column), the gas temperature (middle column), and the azimuthal magnetic field component (right column) at 20 r_g for the three runs. The two black vertical lines in each panel indicate the start and the end of the quasi-steady state, respectively (see Figure 2). The green and blue lines in the density diagrams indicate the positions of the effective absorption and electron-scattering photospheres, respectively, as measured from the rotational axis.

The radiative efficiencies for the outward radiation calculated in the three runs are around a few percent, comparable to the values reported in Jiang et al. (2014a, 2019b). When the mass accretion rate approaches the critical value, the advection of radiative energy becomes more important; $\eta_{\rm R,BH}$ rises from 0.4% in the subcritical case to 1.0% in the near-critical case. Correspondingly, the radiative efficiency drops from 6.1% to ∼3%, since more radiative energy is swallowed by the black hole. The fall in the radiative efficiency with the increasing mass accretion rate is a result of increasing advection and outflows occurring at the same time ($\xi_{\rm w}$ increases slightly from XRB0.8 to XRB0.9). Since the radiation pressure increases with the increasing accretion rate, more gases are lost via true outflows. In XRB0.01, where the mass accretion rate is the lowest among the three runs, no true outflows can be detected. On the other hand, the efficiency of the swallowed kinetic power is always around 20%, having a weak correlation with the accretion rate.

3.5. Spatial Structure of the Disk

We calculate the time- and azimuthally averaged distributions of the density ρ, the radiation energy $E_{\rm R}$, and the gas temperature $T_{\rm gas}$ in the inner region of the disk, and overlay them with the streamlines of the density-weighted flow velocity, radiation flux, and magnetic fields, respectively, in Figure 5. We also calculate the electron scattering and effective absorption optical depth radially from the outer edge (about 1600 r_g) of the simulation box, and identify the photosphere locations where the optical depth reaches unity. Note that here the definition is different from that in Section 3.2, where the integration starts from the rotational axis.

The accretion flows near the disk mid-plane are dominated by inflows in all runs, while strong outflows are formed inside the low-density funnels (the regions encircled by the effective absorption photosphere), with a velocity of ∼0.1c, except in the low–accretion rate case XRB0.01, which has no true outflow. We define the point where the radial velocity v_r changes its sign at the axis as the stagnation point. The stagnation points where the outflows are launched are located at about 20 r_g, which are similar to the super-Eddington AGN case (Jiang et al. 2019b). The disk becomes thicker as the accretion rate increases, which results in a narrower funnel. The effective absorption photosphere also thickens with the increasing accretion rate; its half-opening angle, measured from the disk mid-plane, increases from 20° to 70° when the accretion rate rises from subcritical to near-critical. As already mentioned in Section 3.2, high-temperature coronas can be seen above the effective absorption photospheres inside the low-density funnel regions. The temperatures of the coronas are roughly anticorrelated with the accretion rates. The corona size shrinks when the accretion disk thickens, as a result of narrower funnels.

The radiation energy density peaks near the disk mid-plane. However, in the XRB0.01 case, where the accretion rate is low, it has a relatively lower density in the mid-plane, but peaks at the disk surfaces. Similar distributions have been seen in previous simulations (Jiang et al. 2019a). In the XRB0.8 and XRB0.9 runs, where the radiation luminosity is ∼0.1 $L_{\rm Edd}$, the lab frame radiation flux inside the disk is dominated by the advection term $v_r E_{\rm R}$, while above the disk region, the flux flows out roughly vertically at its local radius. In the low–accretion rate XRB0.01 run, the photons flow out nearly radially through the low-density funnel. We show vertical profiles of the radiation flux divergence in Figure 6, to examine the locations of the energy dissipation. The energy dissipation is enhanced near the disk surface in the XRB0.01 run, but near the disk mid-plane in the other two runs. In other words, the energy dissipation mainly occurs inside the disk when the accretion rate is close to the critical value, but near the disk surface when the accretion rate is low. The energy dissipation is not vertically uniform inside the disk in all three runs, and this differs from the assumption of the Shakura & Sunyaev (1973) model, that the dissipation rate should be independent of the distance from the mid-plane.

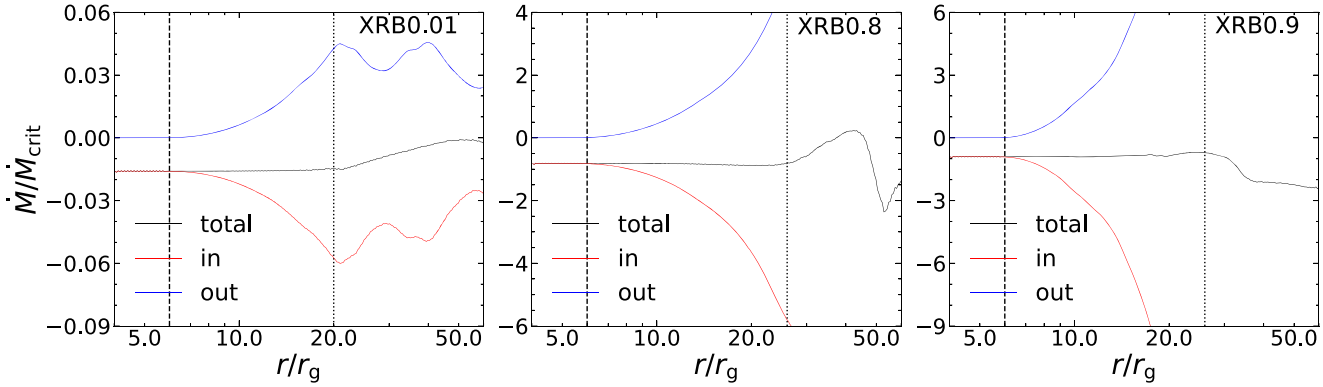

Figure 4. Time-averaged radial profiles of the mass accretion rates normalized to the critical rates. In each panel, the solid black lines show the net mass accretion rates, while the solid blue and red lines show the mass outflow and inflow rates, respectively. The dashed black lines indicate the location of the ISCO (6 $r_{\rm g}$). The dotted black lines indicate the outer radius of the quasi-steady disk.

The magnetic field structure is determined by the initial magnetic field topology. In the runs with multiple magnetic field loops initially (XRB0.01 and XRB0.8), the net radial magnetic fields near the disk mid-plane are induced. In the run with a single magnetic field loop initially (XRB0.9), the net poloidal magnetic fields are produced and thread through the disk. However, we emphasize both magnetic fields are able to produce magnetic pressure–supported disks. The details of the disk pressure profiles will be discussed below, in Sections 3.6 and 3.7.

3.6. Radial Profiles of the Disk

We calculate the time-averaged radial profile of any quantity a as

$$\langle\langle a\rangle\rangle = \frac{\int_0^{2\pi}\int_{\theta_1}^{\theta_2}\int_{t_1}^{t_2} a dt\sin\theta d\theta d\phi}{\Delta t\int_0^{2\pi}\int_{\theta_1}^{\theta_2}\sin\theta d\theta d\phi}, \quad (7)$$

where $\Delta t = t_2 - t_1$ is the time duration of the quasi-steady state and $\theta_{1,2}$ correspond to the range of the bound gas, which has a total energy $E_{\rm t} = \frac{1}{2}\rho v^2 + \frac{\gamma P}{\gamma-1} + \rho\phi + \frac{E_{\rm R}}{3}$ lower than 0. The time- and mass-weighted radial profile of any quantity a is defined as

$$\langle\langle a\rangle\rangle_\rho = \frac{\int_0^{2\pi}\int_{\theta_1}^{\theta_2}\int_{t_1}^{t_2} a\rho dt\sin\theta d\theta d\phi}{\Delta t\int_0^{2\pi}\int_{\theta_1}^{\theta_2}\rho\sin\theta d\theta d\phi}. \quad (8)$$

First, we show the radial profiles of the vertical effective optical depth and the electron-scattering optical depth in the left two panels of Figure 7. The vertical optical depth at a specific radius r is defined as $\tau = \int_0^{\pi}\kappa\rho r d\theta$, where κ is the effective or electron-scattering opacity. The optical depth increases with the increasing disk radius (except for the effective optical depth of the XRB 0.8 run), because of the larger surface density, and also increases with the increasing net mass accretion rate. The optical depth is larger than 10^2, measured vertically, when the accretion rate is close to the critical value in the XRB0.8 and XRB0.9 runs, and it is ∼10 in the low–accretion rate XRB0.01 run. Except for the innermost region near the ISCO in the XRB0.01 run, the disks are always optically thick vertically. We also compare the radial advection timescale of the accretion disk, $\tau_r = r/v_r$, with the estimated vertical escape timescale, $\tau_z = H/v_{{\rm tran},z}$, for the three runs XRB0.01, XRB0.8, and XRB0.9, within 10° of the disk mid-plane, where H is the scale height of the effective absorption photosphere, $v_{\rm tran} = F_{\rm R}/E_{\rm R}$ is the effective energy transport speed, and $v_{{\rm tran},z}$ is the vertical component. The ratio of τ_z/τ_r is shown in the right panel of Figure 7. When the vertical escape timescale exceeds the radial advection timescale, photons will be trapped with the inward gas flow. We note here that $v_{\rm tran}$ is actually higher than the photon diffusion speed, because of the existence of other transport mechanisms, such as magnetic buoyancy. The photon trapping effect becomes important when the mass accretion rate is close to the critical rate, as in the XRB0.8 and XRB0.9 runs, and this effect is greatly enhanced in disk regions inside 10 $r_{\rm g}$. The photon trapping is not important in the XRB0.01 run.

We show mass-weighted radial profiles of the gas pressure $P_{\rm g}$, the isotropic radiation pressure $P_{\rm R} = E_{\rm R}/3$, and the magnetic pressure $P_{\rm B}$ in Figure 8. The magnetic pressure is comparable to or dominant over the radiation pressure in the range from ISCO to 20 $r_{\rm g}$. This is similar to the simulation results for a supermassive black hole (Jiang et al. 2019a). The gas pressure is two to three orders of magnitude lower than the radiation pressure in all runs, consistent with a previous cylindrical simulation (Jiang et al. 2014a). We also show the magnetic pressure contributed by the time-averaged magnetic field over the quasi-steady period, i.e., the nonturbulent component (the dashed blue lines in Figure 8). In the run with initially net poloidal magnetic fields (XRB0.9, with single-loop magnetic fields), the nonturbulent magnetic pressure contributes less than 10%, suggesting that the magnetic pressure is dominated by the turbulent component. For the other two runs (XRB0.01 and XRB0.8, with multi-loop magnetic fields), the total magnetic pressure is dominated by the nonturbulent component.

Radial profiles of the stresses that may account for angular momentum transfer are also shown in Figure 8. We calculate the turbulent component of the Maxwell stress $S_{\rm m} = \langle\langle -B_x B_\phi\rangle\rangle + \langle\langle B_x\rangle\rangle\langle\langle B_\phi\rangle\rangle$, where $B_x = B_r\sin\theta + B_\theta\cos\theta$; the mean magnetic field component of the Maxwell stress $S_{\bar{\rm m}} = -\langle\langle B_x\rangle\rangle\langle\langle B_\phi\rangle\rangle$; and the Reynolds stress $S_{\rm h} = \varsigma\langle\rho v_x v_\phi\rangle\rangle - \langle\langle\rho v_x\rangle\rangle\langle\langle v_\phi\rangle\rangle$, where $v_x = v_r\sin\theta + v_\theta\cos\theta$. Here, the angular momentum carried by the mean inflow in the accretion disk is subtracted for the Reynolds stress. We have $S_{\rm R} = \langle\langle P_{\rm R}^{r\phi}\sin\theta + P_{\rm R}^{\theta\phi}\cos\theta\rangle\rangle$ for the radiation stress. The Maxwell stress is slightly higher than the Reynolds stress for angular momentum transfer, and its magnitude during the quasi-steady state is scaled with the vertical component of the magnetic flux; see Figure 5. Similar phenomena have been

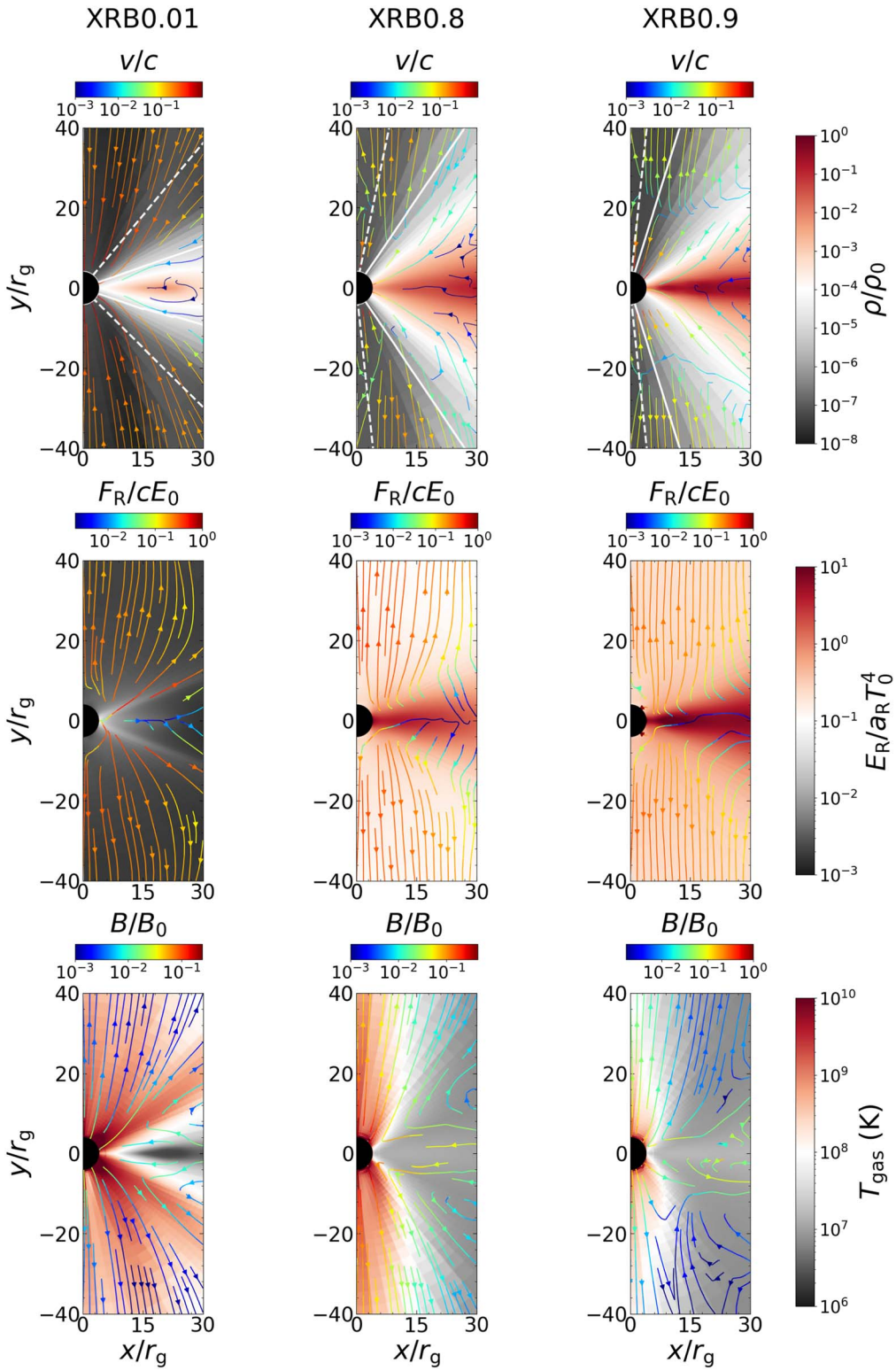

Figure 5. Time- and azimuthally averaged spatial structures of the accretion flows in the three runs. Top row: density (color maps) and mass-weighted flow velocity (streamlines). The solid and dashed white lines represent the photosphere locations for effective absorption and electron scattering, respectively. Second row: radiation energy (color maps) and radiation flux (streamlines). Third row: gas temperature (color maps) and magnetic fields (streamlines).

found in various simulations (Hawley et al. 1995; Bai & Stone 2013; Fromang et al. 2013; Simon et al. 2013; Béthune et al. 2017; Zhu & Stone 2018; Jiang et al. 2019b). In the XRB0.9 run, with net poloidal magnetic fields, the turbulent component of the Maxwell stress is larger than the mean component by an order of magnitude. For the other two runs, XRB0.01 and XRB0.8, there are large mean azimuthal magnetic fields, because of the shearing of the initial radial fields near the disk mid-plane. So the mean-field component of the Maxwell stress is larger than or comparable to the turbulent component. The radiation stress plays

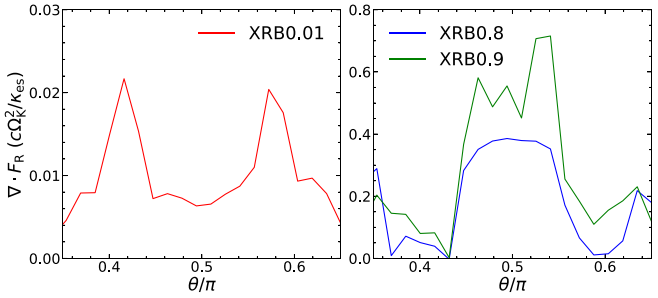

Figure 6. Time-averaged vertical profiles of the radiation flux divergence at $10\,r_g$ for the three runs.

an unimportant role in all three runs, especially when the accretion rate is quite low, which is in contrast with the AGN simulation (Jiang et al. 2019a).

The effective α parameter as a function of radius is shown in the bottom row of Figure 8. The α parameter is found in the range $\sim$0.03–0.2, and it has similar values in the three runs. This is similar to a previous simulation in cylindrical coordinates (Jiang et al. 2014a). The radiation stress has a negligible contribution to the effective α, because the disk is optically thick and the mean free path of the photons is small. As a result, the anisotropic component of the radiation field that is needed to produce angular momentum transfer is greatly suppressed.

3.7. Vertical Profiles of the Disk

Figure 9 shows the vertical (poloidal) structures of the accretion flow at $10\,r_g$ in the three runs. The vertical density profiles of these three runs are similar: all peak at the disk mid-plane and decrease toward the disk surface. The density decreases following an exponential relation $\rho \propto e^{-|z|}$, which is slower than the Gaussian profile $\rho \propto e^{-z^2}$ predicted for the isothermal case, and it is less concentrated on the disk mid-plane compared to the sub-Eddington accreting AGNs in Jiang et al. (2019a).

For the near-critical XRB0.8 and XRB0.9 runs, the gas temperature and the radiation temperature are in thermal equilibrium near the disk mid-plane. They peak at the mid-plane and decrease toward the disk surface. Above the disk surface, the radiation temperature continues to decrease, but the gas temperature starts to increase, and is significantly higher than the radiation temperature in the funnel region. For the subcritical XRB0.01 run, the gas temperature is always higher than the radiation temperature, and the radiation temperature peaks near the disk surface. This is because the effective optical depth of the disk is low ($<$10; see Figure 7). The radiation and gas have not reached local thermal equilibrium.

Although the radiation pressure is comparable to the magnetic pressure, the factor that supports the disk is actually the negative gradient of the pressure from the disk mid-plane to the disk surface. In the XRB0.01 run, the slope of the magnetic pressure is significantly higher than that of the radiation pressure; in the XRB0.8 run, the former is higher than the latter by at least a factor of 2; and in the XRB0.9 run, the former is higher than the latter by a factor of 2 near the disk mid-plane, but they become comparable at large angles. Thus, the disk is mainly supported by the magnetic pressure gradient near the disk mid-plane, which is similar to what was found in the sub-Eddington simulation of an AGN (Jiang et al. 2019a). The radiation pressure gradient becomes important when the accretion rate approaches the critical value, especially at large scale heights.

If the magnetic pressure gradient significantly contributes to supporting an accretion disk vertically, one may expect to see the undulatory Parker instability (Tao & Blaes 2011). To check this, we extract the square of the magnetic Brunt–Väisälä frequency (Blaes et al. 2011), expressed as

$$N_{\rm mag}^2 \equiv g\left(-\frac{g}{c_{\rm t}^2} - \frac{d\ln\rho}{dz}\right), \tag{9}$$

where $g = \Omega^2|z|$ is the approximated acceleration due to the gravity of the central black hole, $c_{\rm t} \equiv [\Gamma_1(P_{\rm g} + P_{\rm R})/\rho]^{1/2}$ is the adiabatic sound speed, and $\Gamma = 4/3$ is the adiabatic index. We show the vertical profiles of $N_{\rm mag}^2/\Omega^2$ for the three runs in Figure 10. The values are negative on both sides near the mid-plane for the XRB0.01 and XRB0.8 runs, suggesting the presence of undulatory Parker modes. We emphasize that the presence of the Parker instability is not inconsistent with the disk being in a quasi-steady state, because the disk is not absolutely steady and the magnetic pressure is averaged over time. For the XRB0.9 run, the values are negative only in a very limited vertical range, probably because the radiation pressure gradient has a non-negligible contribution in this run. For the XRB0.8 run, we display a snapshot of the density at the time $65\,t_0$ in Figure 11. We zoom in on the region near the mid-plane at radii 14–20 r_g to show the density fluctuations caused by the Parker instability inside the disk. Ordered magnetic fields are apparent in low-density regions, while the turbulent component dominates the high-density ones. The magnetic field strength, which is shown by the color of the streamlines, is anticorrelated with the gas density. This is a clear signature of magnetic buoyancy (Blaes et al. 2011; Jiang et al. 2014a, 2019b).

The vertical profiles of the Maxwell and Reynolds stresses have similar shapes: both peak near the disk mid-plane and both decline toward the disk surfaces. The turbulent component of the Maxwell stress has a small dip at the disk mid-plane in the XRB0.01 run, because of the subtraction of the mean-field component. The vertical profile of the radiation stress is different, and shows a bimodal distribution. This is because the anisotropy of the radiation determines the radiation stress, which reaches its maximum when the optical depth is close to unity. A similar bimodal distribution is also seen in sub-Eddington simulations around an AGN (Jiang et al. 2019a), although the radiation stress in our case is not important.

4. Discussion

4.1. Angular Momentum Distribution

The angular momentum distribution reflects how matter is transferred into the central compact object. We plot the density-weighted rotation velocity as a function of radius for the three runs in Figure 12. The disk motion is close to Keplerian outside the ISCO. These results are similar to those obtained from the simulations in cylindrical coordinates (Jiang et al. 2014a). The radial rotation velocities are marginally super-Keplerian in all runs; this is because we have included the motions of the outflows. We show the vertical profiles of the rotation velocity at $10\,r_g$ in the right panel of Figure 12. Near the disk surface,

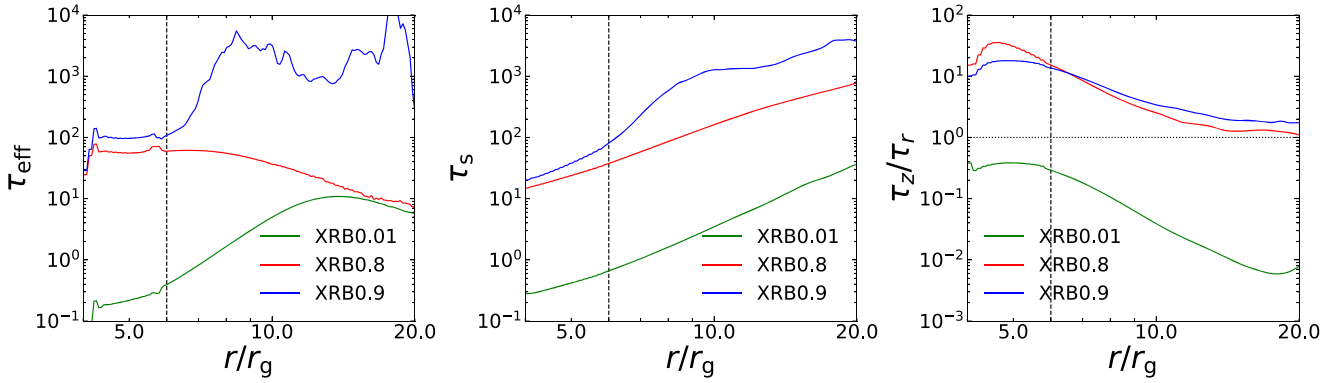

Figure 7. Time-averaged radial profiles of the vertical effective optical depth (left), the electron-scattering optical depth (middle), and the ratio between the vertical escape timescale and the radial advection timescale (right) for the three runs. The vertical dashed line marks the position of the ISCO at 6 $r_{\rm g}$. The horizontal dotted line marks the place where the vertical escape timescale is comparable to the radial advection timescale (i.e., the location where photon trapping is important).

where the outflows form, the flows become super-Keplerian, as the gravitational force cannot balance the centrifugal force. The gas motion is highly super-Keplerian for the XRB0.8 run, and close to Keplerian for the XRB0.9 run, consistent with the presence of the outflows seen in Figure 5. The difference between the XRB0.8 and XRB0.9 runs is caused by the different initial magnetic fields, not by the increasing mass accretion rate, because the trend is opposite to that between the XRB0.01 and XRB0.8 runs. In the XRB0.01 run, there are no true outflows, and the motion above the scattering photosphere is dominated by the inflow of the low-density and low–angular momentum initial density floor (see Figure 5). Below the scattering photosphere, but above the effective absorption photosphere, the accretion gas dominates. This is the reason why the accretion flow is sub-Keplerian at high scale heights. The dominance of the Maxwell and Reynolds stresses over the radiation stresses in the three runs suggests that MRI plays an important role in the angular momentum transfer (Balbus & Hawley 1998).

4.2. Comparison with Theoretical Disk Models

The radiation produced inside the disk is released locally (Figure 5). The disks are nearly Keplerian in the bound gas region (Figure 12). These satisfy the standard disk model assumptions. Contrary to the frequently made assumption that it is constant throughout the disk, the ratio of the vertically integrated r–ϕ stress to the vertically integrated pressure (frequently called α), drops by almost an order of magnitude from the ISCO region, where it is ∼0.2, to 20 $r_{\rm g}$, where it is ∼0.03 (Figure 8). The scale height of a radiation pressure–dominated α disk is determined by $H=\frac{\kappa_{\rm es}\dot{M}}{4\pi c}\left|\frac{d\ln\Omega}{d\ln r}\right|$ in regions away from the innermost radius, as described in Shakura & Sunyaev (1973). The disk scale height near the innermost radius is smaller by a factor of $1-(r_{\rm in}/r)^{1/2}$. With $\dot{M}=0.0158\dot{M}_{\rm crit}$, $0.82\dot{M}_{\rm crit}$, and $0.9\dot{M}_{\rm crit}$, respectively, for the XRB0.01, XRB0.8, and XRB0.9 runs, the corresponding disk scale heights predicted by the α disk model are $H=0.23r_{\rm g}$, $12r_{\rm g}$, and $14r_{\rm g}$, in the same order, independent of disk radius. However, the disks simulated in this work are thicker than the prediction for the α disk model. The scale height of the effective absorption photosphere is proportional to the disk radius, and it will exceed the model prediction at radii $>10\,r_{\rm g}$. The thicker disk is consistent with those obtained from analytic analysis (Begelman & Pringle 2007) and from numerical simulation (Sądowski & Narayan 2016). The standard disk model also ignores the magnetic field and assumes that the disk is gas- or radiation pressure–supported, and it is also predicted to be thermally unstable in the case where the radiation pressure dominates (Shakura & Sunyaev 1976). We find that these disks are actually magnetic pressure–supported (Figure 9). Begelman & Pringle (2007) assume a saturated magnetic pressure $P_{\rm B}\sim\rho c_{\rm s}v_{\rm K}$, according to the saturated Alfvén velocity ($\sqrt{c_{\rm s}v_{\rm K}}$), where $c_{\rm s}$ is the gas sound speed and $v_{\rm K}$ is the Keplerian velocity. As one can see in Figure 8, their $P_{\rm B}$ roughly matches the simulated pressure in XRB0.01 and XRB0.9, and it is lower than that of XRB0.8 by a factor of a few. The radiation efficiency is found to be ∼3%–6%, which is comparable to the prediction for standard disks.

Strong outflows with velocities of $\sim0.1c$ are seen in the XRB0.8 and XRB0.9 runs. Outflows are not included in either the standard or the slim disk models. However, radiation-driven outflows are expected when the luminosity is high, especially when it approaches the Eddington limit (Shakura & Sunyaev 1973; Watarai & Fukue 1999).

4.3. Disk Properties as a Function of Accretion Rate

The three runs allow us to picture the evolution of the accretion flow at different mass accretion rates. We list some of the key properties of the disk as a function of $\dot{m}$ in Table 3. The thickness of the disk ($\theta_{\rm d}$) is defined as the half-opening angle of the effective absorption photosphere, which is also the half-opening angle of the central low-density funnel. The radiative temperatures at the mid-plane ($T_{\rm c}$) and on the effective photosphere ($T_{\rm ph}$) as a function of radius are fitted with a power-law function in the range of 10–20 $r_{\rm g}$, with a correction for zero torque at the innermost radius, i.e., $T(r)\propto r^{p}f^{1/4}$, where $f=1-(6r_{\rm g}/r)^{1/2}$ and p is the power-law index. We also show the angular distributions of the outflow velocities and mass loads, the latter being the mass-loss rate per unit solid angle, in the funnel region for the two runs XRB0.8 and XRB0.9 in Figure 13. The maximum wind velocity ($v_{\rm w}$) is summarized in Table 3, excluding the XRB0.01 run. These relations may help to develop a semi-analytic accretion disk model that takes into account both advection as well as outflows.

As the accretion rate increases, the accretion disk becomes thicker at a given radius, and the radial profile of the radiation temperature becomes flatter, both at the mid-plane and on the effective absorption photosphere. The mid-plane temperature

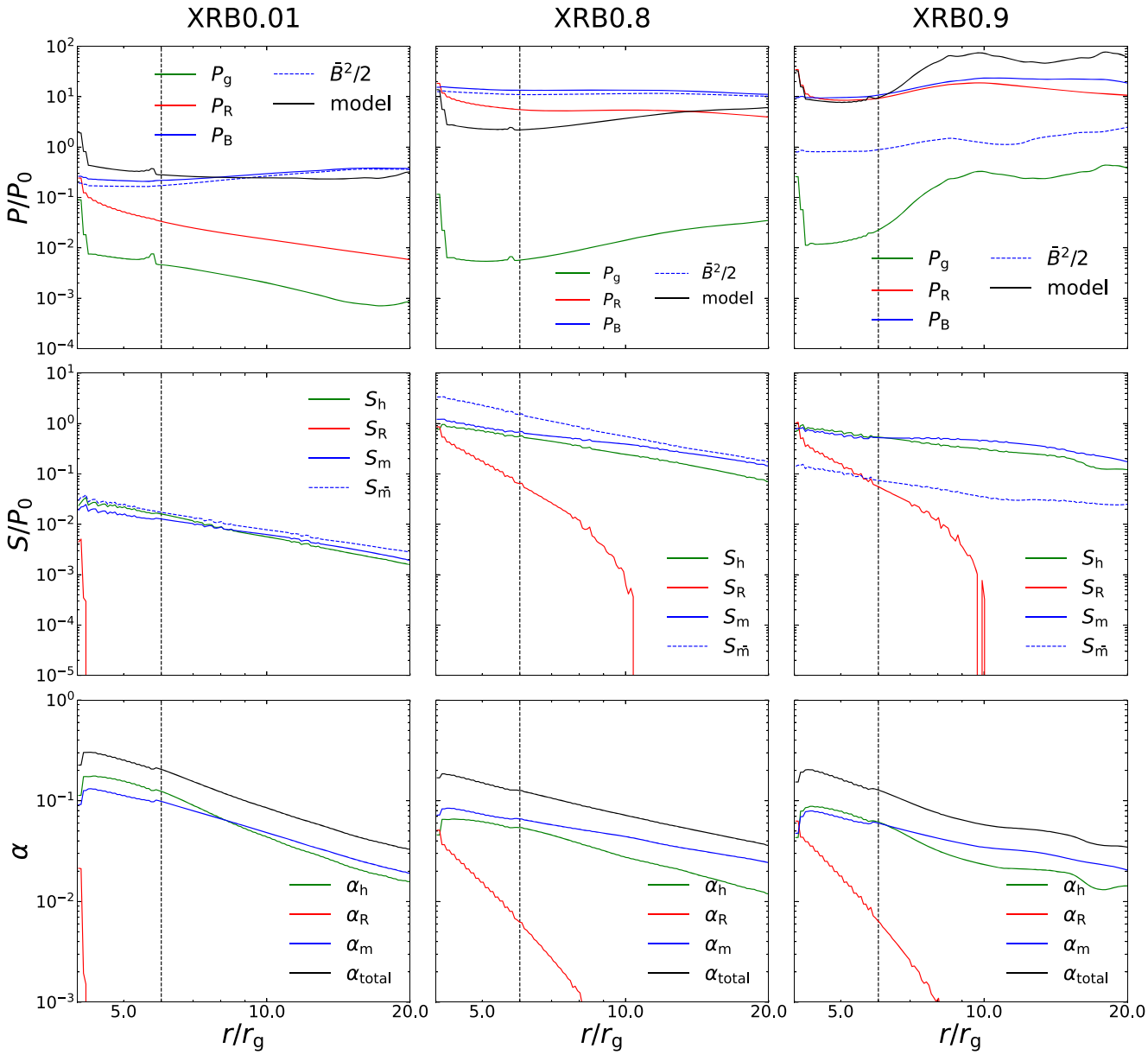

Figure 8. Time-averaged radial profiles of the pressure, stress, and effective α for the three runs. Top row: mass-weighted radial profiles of the gas (green), radiation (red), and magnetic (blue) pressures. The dashed blue line shows the magnetic pressure due to the mean magnetic field. The solid black line indicates the magnetic pressure quoted from Begelman & Pringle (2007). Middle row: radial profiles of the Reynolds (green), radiation (red), and Maxwell (blue) stresses. The dashed blue line shows the Maxwell stress of the mean magnetic field. Bottom row: radial profiles of the effective α parameter due to the Reynolds (green), radiation (red), and Maxwell (blue) stresses, as well as the total (black). The vertical dashed line marks the position of the ISCO at 6 r_g.

profile in the XRB0.9 run appears not to follow such a trend, but becomes steeper than that of the XRB0.8 run, because it cannot be well described by the radial model. The temperature profiles are all flatter than that predicted by the standard accretion disk ($p = -0.75$), but close to that predicted by the slim disk ($p = -0.5$), except for T_c in XRB0.8 and T_{ph} in XRB0.9, which may be a result of strong advection in the accretion flow. We adopt the gas temperature at $10\,r_g$ on the rotational axis as an estimation of the corona temperature (T_{axis}). The corona cools with an increasing accretion rate, with temperatures of 3×10^9 K, 2×10^9 K, and 8×10^8 K, respectively, in the XRB0.01, XRB0.8, and XRB0.9 runs. The radiation efficiency depends weakly upon the accretion rate. It decreases by a factor of 2 when the accretion rate increases from 1% to 80%–90% of the critical value. Also, as the accretion rate increases, more outflows are launched, and thus the outflow to net inflow rate increases with the increasing accretion rate. The outflow velocity is $\sim 0.1c$ and does not seem to vary with the accretion rate. For the two near-critical runs (XRB0.8 and XRB0.9), the outflow velocity decreases with the increasing inclination angle (θ), while the mass load increases with it. As a result, an observer along the funnel edge sees more outflows than one along the rotational axis.

4.4. Outflows

In Table 3, we show that in the near-critical XRB0.8 and XRB0.9 runs, the rate for the true outflows that will escape to infinity is $\sim 0.02\,\dot{M}_{crit}$. The ratio of the true outflow rate to the net mass accretion rate is $\sim$3%. In the large-scale RHD simulations for supercritical accretion (Kitaki et al. 2021), it has

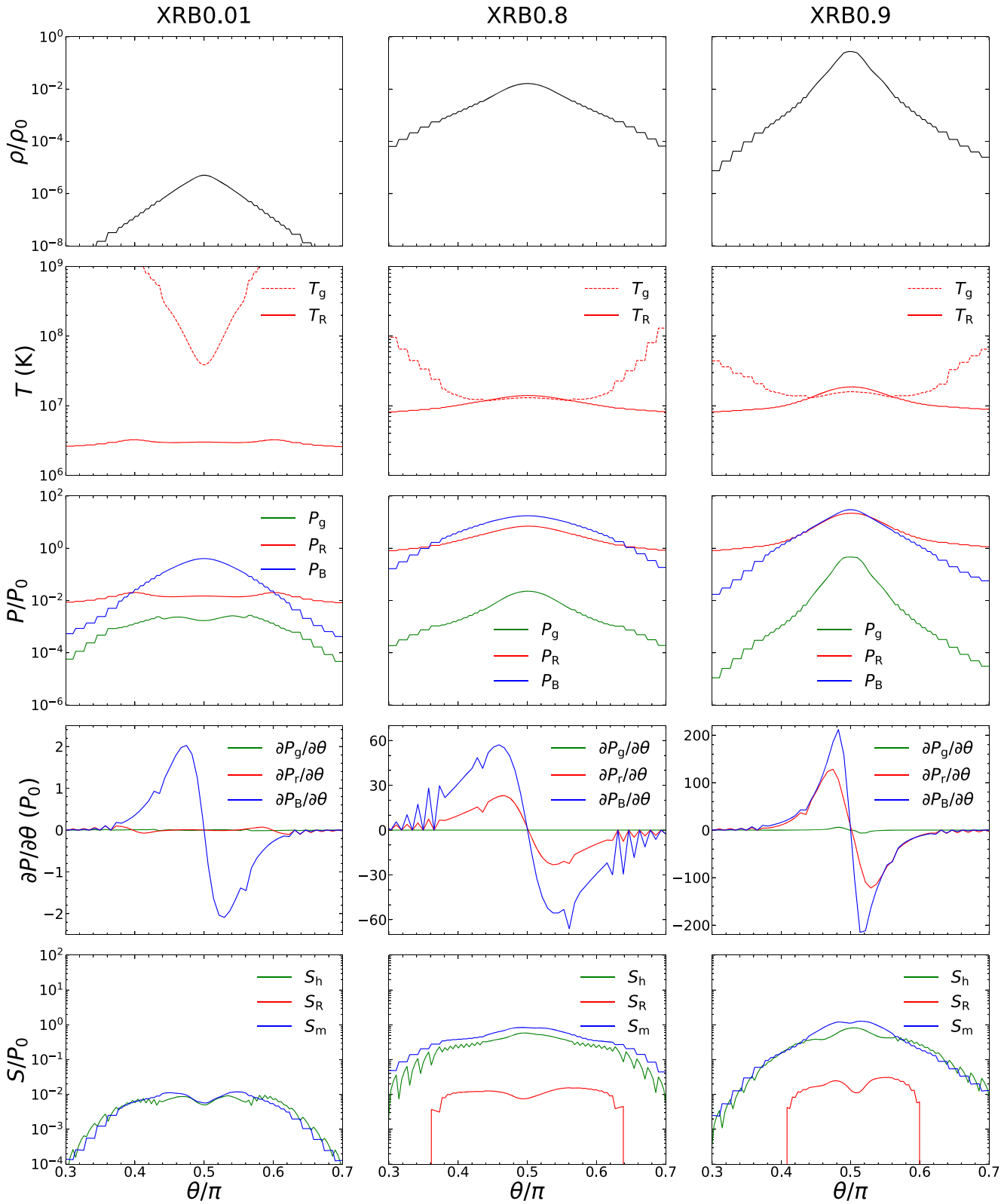

Figure 9. Vertical profiles of the densities, temperatures, pressures, pressure gradients, and stresses at 10 r_g in the three runs. Top row: vertical profiles of the gas density ρ. Second row: vertical profiles of the gas temperature T_g (dashed red) and the radiation temperature T_R (solid red). Third row: vertical profiles of the gas pressure P_g (green), the radiation pressure P_R (red), and the magnetic pressure P_B (blue). Fourth row: vertical profiles of the gas pressure gradient $\partial P_g/\partial\theta$ (green), the radiation pressure gradient $\partial P_R/\partial\theta$ (red), and the magnetic pressure gradient $\partial P_B/\partial\theta$ (blue). Bottom row: vertical profiles of the Reynolds stress S_h (green), the radiation stress S_R (red), and the Maxwell stress S_m (blue).

been found that the true outflow rate is $2.4\,\dot{M}_{\rm crit}$, given a supercritical net mass accretion rate of $18\,\dot{M}_{\rm crit}$ (converted according to our definition). Their ratio of the true outflow rate to the net mass accretion rate is ∼13%, which is consistent with the trend that we show in Table 3, of the ratio growing with the increasing net accretion rate.

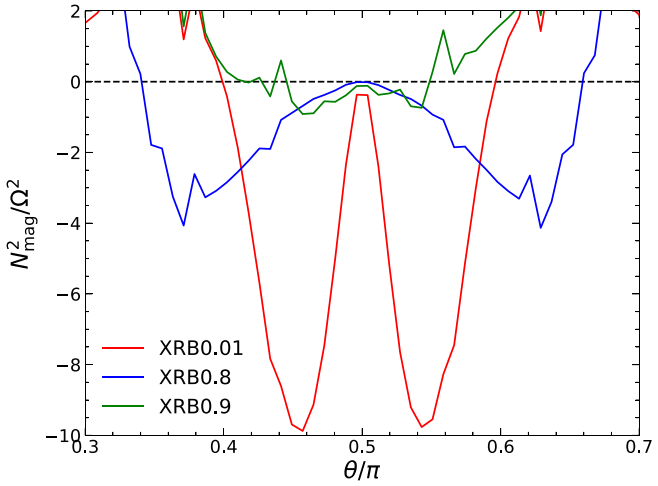

Figure 10. Vertical profiles of the square of the magnetic Brunt–Väisälä frequency at 10 r_g for the three simulation runs.

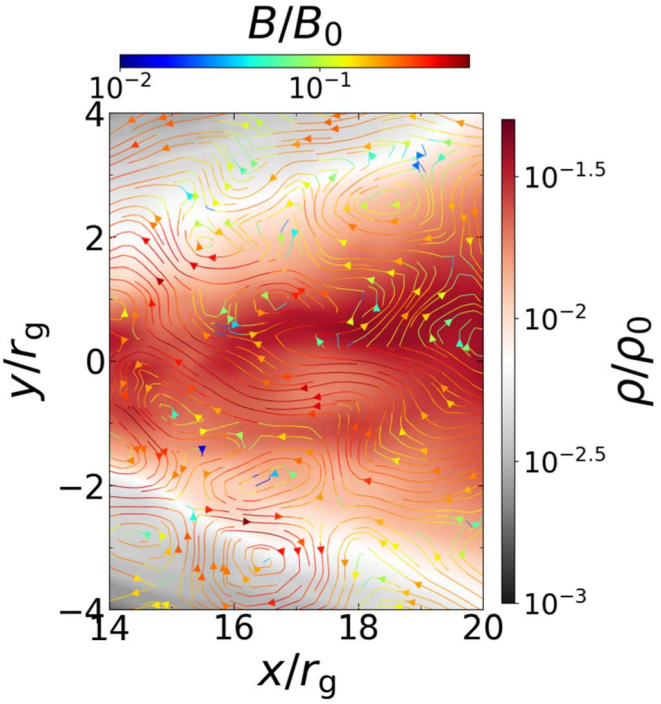

Figure 11. Snapshot of the density for the XRB0.8 run at the time 65 t_0, overlaid with magnetic field lines.

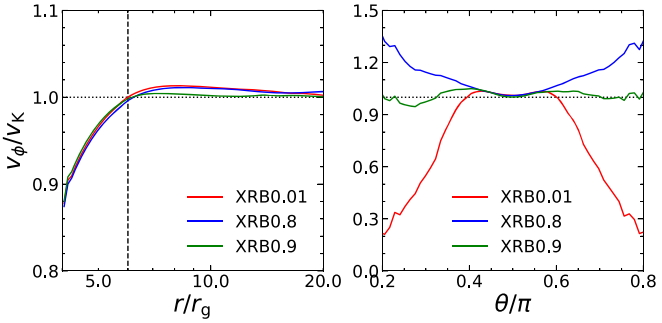

Figure 12. Radial (left) and vertical (right) profiles of the density-weighted rotation velocity v_ϕ, scaled with the Keplerian velocity v_K. The black dashed line in the left panel marks the position of the ISCO at 6 r_g.

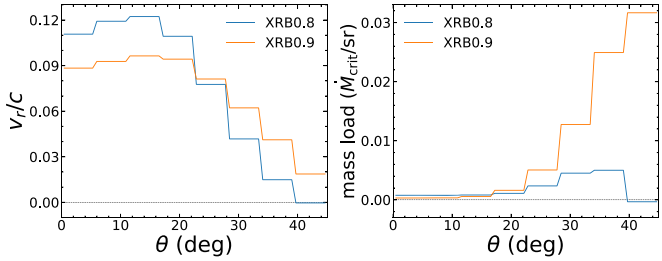

Figure 13. Angular distributions of the outflow velocities and mass loads in the XRB0.8 and XRB0.9 runs.

5. Conclusions

In this paper, we present results from 3D global RMHD simulations of accretion onto a 6.62 $M_\odot$ black hole, with different initial magnetic configurations and, consequently, different accretion rates, from a few percent to $\sim\dot{M}_{\rm crit}$. The main results are summarized below.

Outflows start from the ISCO and the mass-loss rate increases rapidly with the radius. We see no outflows when the accretion rate is about 10^{-2} $\dot{M}_{\rm crit}$. The true outflow to net accretion rate is around 2.5%, when the net accretion rate becomes close to the critical rate. The ratio of the true outflow rate to the net mass accretion rate increases with the mass accretion rate. The peak velocity of the outflow is about 0.1 c, and the mass load of the outflow is peaked near the disk surface.

In the near-critical accretion flow, the energy dissipation occurs mainly inside the disk, while in the subcritical case, the energy dissipates mainly at the disk surface. The radial velocity is more than 10 times the vertical photon diffusion speed in the XRB0.8 and XRB0.9 runs, meaning that photon trapping is important in the near-critical accretion flow. The ratio of the radial velocity to the vertical photon diffusion speed increases with the increasing accretion rate, indicating that the photon trapping effect is more obvious when the mass accretion rate is higher. The radiation efficiency is a few percent, and it depends weakly upon the accretion rate. It decreases by a factor of 2 when the accretion rate increases from 1% to 80%–90% of the critical value.

The disk is dominated by magnetic pressure. The magnetic pressure is larger than or comparable to the radiation pressure. The negative vertical gradient of the magnetic pressure is significantly larger, or at least larger by a factor of 2, than the radiation pressure within a few scale heights of the mid-plane, indicating that the disk is magnetic pressure–supported vertically. The value of the magnetic pressure can be roughly described by the saturated magnetic pressure, as presented in Begelman & Pringle (2007). The Maxwell and Reynolds stresses are the main sources of angular momentum transfer, which contrasts with the AGN case, where the radiation stress plays an important role (Jiang et al. 2019a).

We thank the anonymous referee for the useful comments that helped to improve the manuscript. H.F. acknowledges funding support from the National Key R&D Project, under grant No. 2018YFA0404502; the National Natural Science Foundation of China, under grant Nos. 12025301 and 11821303; and the Tsinghua University Initiative Scientific Research Program. An award of computer time was provided by the Innovative and Novel Computational Impact on Theory and Experiment (INCITE) program. This research used the

resources of the Argonne Leadership Computing Facility, which is a DOE Office of Science User Facility, supported under Contract DE-AC02-06CH11357. Part of this work was performed using resources that were provided by the Cambridge Service for Data Driven Discovery (CSD3), operated by the University of Cambridge Research Computing Service (www.csd3.cam.ac.uk), provided by Dell EMC and Intel, using Tier-2 funding from the Engineering and Physical Sciences Research Council (capital grant EP/T022159/1), and DiRAC funding from the Science and Technology Facilities Council (www.dirac.ac.uk). The Center for Computational Astrophysics at the Flatiron Institute is supported by the Simons Foundation. J.S. acknowledges support from NASA TCAN grant No. 80NSSC21K0496. M.M. acknowledges support via an STFC consolidated grant (ST/V001000/1). S.W.D. acknowledges support from NASA Astrophysics Theory Program grant No. 80NSSC18K1018.

ORCID iDs

Jiahui Huang https://orcid.org/0000-0001-8674-2336
Yan-Fei Jiang (姜燕飞) https://orcid.org/0000-0002-2624-3399
Hua Feng https://orcid.org/0000-0001-7584-6236
Matthew J. Middleton https://orcid.org/0000-0002-8183-2970

References

Abramowicz, M. A., Czerny, B., Lasota, J. P., & Szuszkiewicz, E. 1988, ApJ, 332, 646
Asahina, Y., & Ohsuga, K. 2022, ApJ, 929, 93
Bai, X.-N., & Stone, J. M. 2013, ApJ, 767, 30
Balbus, S. A., & Hawley, J. F. 1991, ApJ, 376, 214
Balbus, S. A., & Hawley, J. F. 1998, RvMP, 70, 1
Begelman, M. C., & Pringle, J. E. 2007, MNRAS, 375, 1070
Béthune, W., Lesur, G., & Ferreira, J. 2017, A&A, 600, A75
Blackman, E. G. 2012, PhyS, 86, 058202
Blaes, O., Krolik, J. H., Hirose, S., & Shabaltas, N. 2011, ApJ, 733, 110
Blandford, R. D., & Znajek, R. L. 1977, MNRAS, 179, 433
Brandenburg, A., Nordlund, A., Stein, R. F., & Torkelsson, U. 1995, ApJ, 446, 741
Das, U., Begelman, M. C., & Lesur, G. 2018, MNRAS, 473, 2791
Davis, S. W., Stone, J. M., & Pessah, M. E. 2010, ApJ, 713, 52
Davis, S. W., & Tchekhovskoy, A. 2020, ARA&A, 58, 407
De Villiers, J.-P., Hawley, J. F., & Krolik, J. H. 2003, ApJ, 599, 1238
Done, C., Gierlinski, M., & Kubota, A. 2007, A&ARv, 15, 1
Esin, A. A., McClintock, J. E., & Narayan, R. 1997, ApJ, 489, 865
Fragile, P. C., Etheridge, S. M., Anninos, P., Mishra, B., & Kluzniak, W. 2018, ApJ, 857, 1
Fragile, P. C., Olejar, A., & Anninos, P. 2014, ApJ, 796, 22
Fromang, S., Latter, H., Lesur, G., & Ogilvie, G. I. 2013, A&A, 552, A71
Galeev, A. A., Rosner, R., & Vaiana, G. S. 1979, ApJ, 229, 318
Gilfanov, M. 2004, MNRAS, 349, 146
Hashizume, K., Ohsuga, K., Kawashima, T., & Tanaka, M. 2015, PASJ, 67, 58
Hawley, J. F. 2001, ApJ, 554, 534
Hawley, J. F., Gammie, C. F., & Balbus, S. A. 1995, ApJ, 440, 742
Hawley, J. F., Guan, X., & Krolik, J. H. 2011, ApJ, 738, 84
Hawley, J., & Krolik, J. 2001, ApJ, 548, 348
Hawley, J. F., Richers, S. A., Guan, X., & Krolik, J. H. 2013, ApJ, 772, 102
Hogg, J. D., & Reynolds, C. S. 2016, ApJ, 826, 40
Hogg, J. D., & Reynolds, C. S. 2018, ApJ, 854, 6
Jeon, M., Pawlik, A. H., Bromm, V., & Milosavljević, M. 2014, MNRAS, 440, 3778
Jiang, Y.-F. 2021, ApJS, 253, 49
Jiang, Y.-F., Blaes, O., Stone, J. M., & Davis, S. W. 2019a, ApJ, 885, 144
Jiang, Y.-F., Stone, J. M., & Davis, S. W. 2013, ApJ, 778, 65
Jiang, Y.-F., Stone, J. M., & Davis, S. W. 2014a, ApJ, 796, 106
Jiang, Y.-F., Stone, J. M., & Davis, S. W. 2014b, ApJ, 784, 169
Jiang, Y.-F., Stone, J. M., & Davis, S. W. 2019b, ApJ, 880, 67
Kawashima, T., Ohsuga, K., Mineshige, S., et al. 2009, PASJ, 61, 769
Kinch, B. E., Noble, S. C., Schnittman, J. D., & Krolik, J. H. 2020, ApJ, 904, 117
Kitaki, T., Mineshige, S., Ohsuga, K., & Kawashima, T. 2017, PASJ, 69, 92
Kitaki, T., Mineshige, S., Ohsuga, K., & Kawashima, T. 2018, PASJ, 70, 108
Kitaki, T., Mineshige, S., Ohsuga, K., & Kawashima, T. 2021, PASJ, 73, 450
Koide, S. 2003, PhRvD, 67, 104010
Kosec, P., Pinto, C., Reynolds, C. S., et al. 2021, MNRAS, 508, 3569
Krawczynski, H., Muleri, F., Dovčiak, M., et al. 2022, Sci, 378, 650
Long, X., Feng, H., Li, H., et al. 2022, ApJL, 924, L13
Markoff, S., Nowak, M. A., & Wilms, J. 2005, ApJ, 635, 1203
McKinney, J. C., & Gammie, C. F. 2004, ApJ, 611, 977
McKinney, J. C., Tchekhovskoy, A., Sadowski, A., & Narayan, R. 2014, MNRAS, 441, 3177
Meyer, F., & Meyer-Hofmeister, E. 1994, A&A, 288, 175
Middleton, M. J., Walton, D. J., Fabian, A., et al. 2015, MNRAS, 454, 3134
Middleton, M. J., Walton, D. J., Roberts, T. P., & Heil, L. 2014, MNRAS, 438, L51
Miller, K. A., & Stone, J. M. 2000, ApJ, 534, 398
Mineo, S., Gilfanov, M., & Sunyaev, R. 2012, MNRAS, 419, 2095
Morales Teixeira, D., Avara, M. J., & McKinney, J. C. 2018, MNRAS, 480, 3547
Neilsen, J., & Lee, J. C. 2009, Natur, 458, 481
Noble, S. C., Krolik, J. H., & Hawley, J. F. 2009, ApJ, 692, 411
Ogawa, T., Mineshige, S., Kawashima, T., Ohsuga, K., & Hashizume, K. 2017, PASJ, 69, 33
Ohsuga, K. 2006, ApJ, 640, 923
Ohsuga, K., & Mineshige, S. 2011, ApJ, 736, 2
Ohsuga, K., Mineshige, S., Mori, M., & Kato, Y. 2009, PASJ, 61, L7
Paczyński, B., & Wiita, P. J. 1980, A&A, 88, 23
Pariev, V. I., Blackman, E. G., & Boldyrev, S. A. 2003, A&A, 407, 403
Pessah, M. E., & Psaltis, D. 2005, ApJ, 628, 879
Pinto, C., Middleton, M. J., & Fabian, A. C. 2016, Natur, 533, 64
Poutanen, J., Lipunova, G., Fabrika, S., Butkevich, A. G., & Abolmasov, P. 2007, MNRAS, 377, 1187
Remillard, R. A., & McClintock, J. E. 2006, ARA&A, 44, 49
Salvesen, G., Armitage, P. J., Simon, J. B., & Begelman, M. C. 2016a, MNRAS, 460, 3488
Salvesen, G., Simon, J. B., Armitage, P. J., & Begelman, M. C. 2016b, MNRAS, 457, 857
Schnittman, J. D., Krolik, J. H., & Noble, S. C. 2013, ApJ, 769, 156
Shafee, R., McKinney, J. C., Narayan, R., et al. 2008, ApJL, 687, L25
Shakura, N. I., & Sunyaev, R. A. 1973, A&A, 24, 337
Shakura, N. I., & Sunyaev, R. A. 1976, MNRAS, 175, 613
Shi, J., Krolik, J. H., & Hirose, S. 2010, ApJ, 708, 1716
Simon, J. B., Bai, X.-N., Armitage, P. J., Stone, J. M., & Beckwith, K. 2013, ApJ, 775, 73
Simon, J. B., Beckwith, K., & Armitage, P. J. 2012, MNRAS, 422, 2685
Sądowski, A. 2016, MNRAS, 459, 4397
Sądowski, A., & Narayan, R. 2016, MNRAS, 456, 3929
Sądowski, A., Narayan, R., Tchekhovskoy, A., et al. 2015, MNRAS, 447, 49
Sorathia, K. A., Reynolds, C. S., Stone, J. M., & Beckwith, K. 2012, ApJ, 749, 189
Stone, J. M., Hawley, J. F., Gammie, C. F., & Balbus, S. A. 1996, ApJ, 463, 656
Stone, J. M., Tomida, K., White, C., & Felker, K. G. 2019, Athena++: Radiation GR magnetohydrodynamics code, Astrophysics Source Code Library, ascl:1912.005
Takahashi, H. R., Ohsuga, K., Kawashima, T., & Sekiguchi, Y. 2016, ApJ, 826, 23
Tao, T., & Blaes, O. 2011, ApJ, 742, 8
Watarai, K.-y., & Fukue, J. 1999, PASJ, 51, 725
Watarai, K.-y., Mizuno, T., & Mineshige, S. 2001, ApJL, 549, L77
Wielgus, M., Lančová, D., Straub, O., et al. 2022, MNRAS, 514, 780
Yuan, F., & Narayan, R. 2014, ARA&A, 52, 529
Zhu, Z., & Stone, J. M. 2018, ApJ, 857, 34